Numerical investigation of erosion of tube sheet and tubes of a shell and tube heat exchanger

Weimin Gao [a,b,*], Yungang Li [a], Lingxue Kong [b]

[a] School of Metallurgy and Energy, North China University of science and Technology, Tangshan, 063009, China
[b] Institute for Frontier Materials, Deakin University, Geelong, VIC, 3216, Australia

ABSTRACT

The failure of shell and tube heat exchangers caused by solid particle erosion has been a major problem in the oil and gas and other industries. Predicting erosion is still a developing art, an accurate simulation method is then significant to analyze the erosion characteristics in such complex geometry and determine erosion rate of metal surface. In this work a physical model was proposed to simulate the erosion of two-pass shell and tube heat exchangers with computational fluid dynamics. The simulation was performed for different feed fluid rates and a range of sand particle sizes from 0.1 to 1000 μm. The erosion rates of tube sheet, tube ends in the inlet plenum and the inner wall of tubes were monitored and the influences of flow pattern, particle size and particle behaviors on erosion were studied. The predictions are compared with the earlier studies and a good agreement was found. The particles can be classified into three groups based on the dependence of erosion rates of tube sheet and tubes on the particle size. The large particles (>200 μm) exhibited a near-linear influence on the erosion rates. The small particles (about 50–200 μm) produced approximate size-independence facet-average erosion rate of tubes, but the maximum local erosion rates of the tubes and tube sheet sharply increased with the decrease of particle size. The fine particles (<about 50 μm) resulted in low facet-average erosion rates but very high local erosion rate. The erosion at the tube sheet, tube end and tube surface also show different aspects of relation with particle size.

© 2016 Elsevier Ltd. All rights reserved.

1. Introduction

Shell and tube heat exchangers are widely used for cooling and heat recovery in oil and gas production and other chemical processes. Erosion is one of major problems of the heat exchangers, when either fluid flowing through tubes or fluid passing through the shells contains solid particles, for instance, seawater is utilized for cooling, and runs at a velocity that likely causes the metal wear from the tube surfaces at its operating temperature (Kuźnicka, 2009; Lai and Bremhorst, 1979). The impingement of solid particles most often occurs on the inside surface of the tubes and near the tube entrances for shell and tube heat exchangers and also along the U bend for U-tube heat exchangers. Severe metal loss in some local areas of a heat exchanger not only requires frequent maintenance but also results in the failure of the heat exchanger, leading to

very costly planned and unplanned maintenance, production loss and potentially environmental disasters.

Erosion process has been investigated extensively since decades with respect to the mechanism (Research and Markets, 2011) and the relationship between the amount of erosion and the variables dominating the erosion, including the materials of targets (Laguna-Camacho et al., 2013), fluid properties and velocity (Kesana et al., 2013a,b), properties and velocity of the solid particles (Kesana et al., 2013a,b), and temperature (Naz et al., 2015). Despite these fundamental studies and recent advances in computational fluid dynamics the erosion process has yet to be fully predicted with reasonable accuracy even for fairly dilute suspension of solid particles. Most prediction studies mainly concern the erosions on simple geometries, such as straight and sudden contraction tubes (Badr et al., 2005; Duwig et al., 2008; Habib et al., 2007, 2008), elbows (Chen et al., 2004; Mazumder et al., 2008; Njobuenwu and Fairweather, 2012; Safaei et al., 2014; H. Zhang et al., 2012), tees (Chen et al., 2004), U bends, orifices (Nemitallah et al., 2014), pipe and wall cavities (Lin et al., 2014; Wong and Solnordal, 2012; Wong et al., 2013a,b) and flat plates (Wong et al., 2012). Predicting the erosion process in shell and tube heat exchanger is more
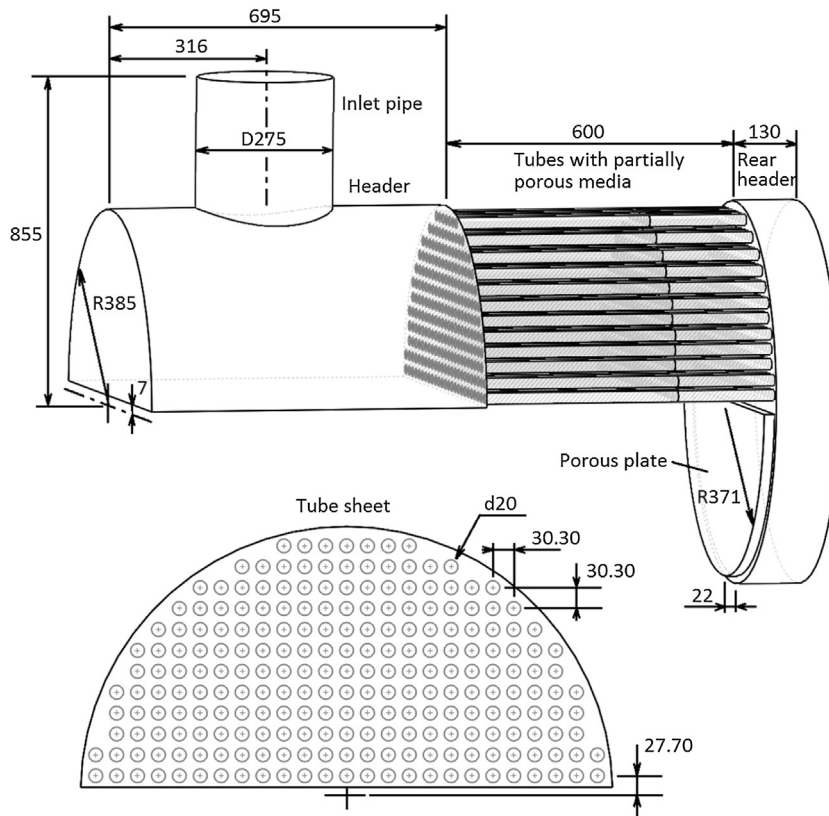
Fig. 1. The main dimensions of the model for a shell and tube heat exchanger and the tube sheet indicating the arrangement of tubes (dimensions are in mm).

challenging because of the complexity of flow field in the regions likely to be worn, i.e., the inlet head and the downstream regions from the tube entrances. A single fluid stream expands into a large area and then divides into multiple smaller streams; turbulence leads to a very high velocity in some local regions. The flow field much depends on the geometry of the heat exchanger and the properties and velocity of the fluid.

The tube entrance of shell and tube heat exchanger is the most critical region with respect to erosion failure. The rate of erosion greatly relates to the flow characteristics in this region. It has been found that a cross flow pattern near some tube inlets considerably contributed to the erosion of the tubes (Bremhorst and Lai, 1979). Low velocity caused accumulation of deposits, reduction of tube diameter and sometimes complete blockage of tubes (Ranjbar, 2010). The effects of flow velocity and sand particle size on the rate of erosion in a shell and tube heat exchanger were investigated numerically (Habib et al., 2006, 2005), where k-ε turbulence model was used for fluid and the Lagrangian approach was employed for tracking particles. The influence of particle motion on the fluid flow field was neglected. Half of the heat exchanger having 38 tubes were considered based on the assumption of symmetrical flow. However, both experimental and numerical studies of a sudden symmetric expansion flow (Bremhorst and Lai, 1979; Duwig et al., 2008; Sugawara et al., 2005; Ternik, 2009; Velasco et al., 2008) have shown that the flow field is asymmetry, which is attributed to the competing effects of shear thinning and inertia on the size of the corner vortex (Mishra and Jayaraman, 2002). The asymmetric flow in the head of shell and tube heat exchanger is similar in nature to asymmetries noticed in plane expansion flow. A full geometry was used in the modelling of flow field in the symmetrical head of a shell and tube heat exchanger (Bremhorst and Brennan, 2011). In the modelling, the Reynolds-Averaged Navier–Stokes (RANS) equations for continuity and momentum equations and the SST-k-ω

turbulence model were used. The prediction of erosion/corrosion of the tube inlets was based on the characteristics of flow field as solid particles were not included in the modelling. Accurate prediction of erosion rate depends on the determination of the particle impact velocity, impingement angle and the frequency of impacts on concerned surfaces. These particle variables can be derived from their trajectories. The Lagrangian approach has been demonstrated in modelling particle motion in various geometries for dilute systems (Badr et al., 2006; Parsi et al., 2014; Wong et al., 2013a,b).

Although erosion of tube sheet, tubes and tube ends is a common problem that influences the performance of shell and tube heat exchangers, there is no research published in the literature that deals with the effect of various parameters on the erosion of these targets. The present work aims to study the erosion at the entrance region and tubes of the heat exchanger and the effect of particle behaviors and fluid flow on the rate of erosion. A physical model is proposed based on initial computational fluid dynamics simulation of fluid flow in a shell and tube heat exchanger, which provides the flow characteristics in the heat exchanger and the dependence of results on the momentum and turbulence models adopted. The simulation is performed for different feed fluid rates and particle sizes in a range of 0.1–1000 μm.

2. Model description

2.1. Physical model

The simulations were performed for the inlet head inside and the flow development regions in tubes close to the tube sheet of a typical shell and tube heat exchanger with two-pass construction. Fig. 1 shows the geometry of the physical model. Fluid enters from the side entry into the head and then is distributed into 230 tubes at the tube sheet. The liquid through each tube first experiences a
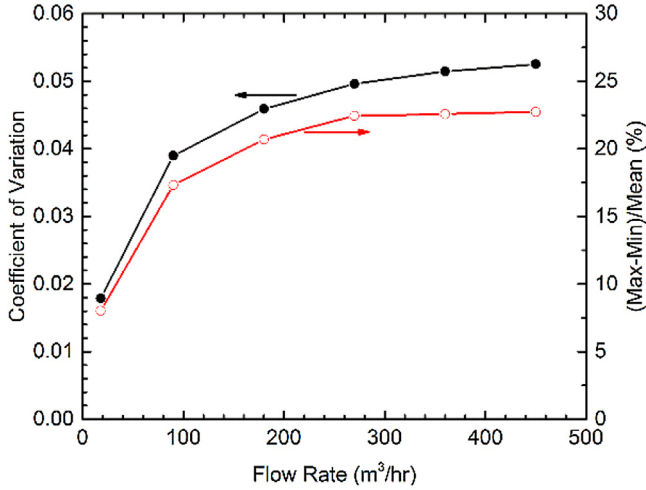
Fig. 2. The uniformity of fluid flow through tubes. The coefficient of variation is the ratio of the standard deviation of flow rate through tubes to the mean. The abscissa is the flow rate of feed fluid.

400 mm pipe flow and then a 200 mm porous flow. In another word, first 400 mm from the tube sheet of each tube is a pipe and the last 200 mm is defined as a porous media zone, where the porous parameters were adjusted to produce the same pressure drop as the full length tube of the first pass. The fluid from the tube bundle runs into the rear head and finally flows out from the porous plate zone, which was designed to give a similar pressure drop to the second pass.

The approach of a short tube with a porous plug at the tube end greatly reduced the number of computational elements (nodes). The porous parameters of viscous resistance and inertia resistance factors were determined from the pressure drop of full length tubes at various velocities, so that the modelling results can well represent the heat exchanger with the entire tube bundle. Another important merit of this approach is its capability in properly simulating the flow field in the tube entrances and in the flow development section of every tube, where severe tube wear is likely to occur at. There are a few other porous media approaches that have been used to simply the simulation of large scale tubular heat exchanger (Bhutta et al., 2012; Bremhorst and Brennan, 2011; Shi et al., 2010). It has been demonstrated that extending porous media (at one side or at both sides of media zone) with a short tube predicted more accurate flow distribution than the conventional porous media approach (Bremhorst and Brennan, 2011; Shi et al., 2010).

The flow rate through each tube depends on the total feed rate and the position of the tube entrance in the head. In general, the difference in flow rate between different tubes is small and ignored, when the exchanger runs at high feed rates and the tubes are long enough to produce a high flow resistance that can lead to a uniform pressure over the tube sheet in the head. Initially the flow in the entire heat exchanger was simulated with a model containing two sets of porous media (with tubes) zone, the outlet head and the rear head. The two sets of porous media zone represent the two tube bundles (the first pass and the second pass), respectively. The flow rate through each tube, q, was calculated. It was found that the flow rate difference among the first pass tubes was up to 20% (($q_{max}-q_{min}$)/q_{mean}) for tubes of 5 m in length at feed liquid rate of 180 m^3/hr, as shown in Fig. 2. Pressure deviation was also found between tube outlets in the rear head, indicating the effect of backpressure in the rear head on the distribution of fluid through the tube bundle. So that in the present work the rear head and a near semi-circle plate porous media were included into the physical model. The parameters of the plate porous media was adjusted

to produce a pressure drop as the same as that of the entire second pass tube bundle.

2.2. Liquid flow modelling

In the head of the heat exchanger, partial separating flow and adverse pressure gradients may occur reality, due to the rapid expansion from inlet pipe to the head plenum and the large variation in flow direction at the tube entrances. In the present work, the Reynolds Averaged Navier–Stokes (RANS) equations, Eqs. (1) and (2), and SST-k-ω turbulence model, Eqs. (3) and (4), were then used for the continuum. Initially steady flow equations were solved for the domain. Due to the relatively high value and fluctuation of residuals of k and ω, the simulation was then switched to solve the transient equations. The simulation approach will be discussed in details in the simulation details.

$$\frac{\partial u_i}{\partial x_i} = 0 \tag{1}$$

$$\frac{\partial u_i}{\partial t} + u_j \frac{\partial u_i}{\partial x_j} = -\frac{1}{\rho}\frac{\partial p}{\partial u_i} + \frac{\partial}{\partial x_j}\left(2(v+v_T)S_{ji}\right) + g_i \tag{2}$$

$$\frac{\partial k}{\partial t} + u_j \frac{\partial k}{\partial x_j} = -\overline{u_i' u_j'}\frac{\partial u_i}{\partial x_j} - \beta^* k\omega + \frac{\partial}{\partial x_j}\left[(v+\sigma_k v_T)\frac{\partial k}{\partial x_j}\right] \tag{3}$$

$$\frac{\partial \omega}{\partial t} + u_j \frac{\partial \omega}{\partial x_j} = -\alpha\frac{\omega}{k}\overline{u_i' u_j'}\frac{\partial u_i}{\partial x_j} - \beta\omega^2 + \frac{\partial}{\partial x_j}\left[(v+\sigma_w v_T)\frac{\partial \omega}{\partial x_j}\right] + 2(1-F_1)\sigma_{\omega2}\frac{1}{\omega}\frac{\partial k}{\partial x_i}\frac{\partial \omega}{\partial x_i} \tag{4}$$

where

$$v_T = \frac{a_1 k}{\max(a_1\omega, SF_2)}$$

$$F_1 = \tanh\left\{\left\{\min\left[\max\left(\frac{\sqrt{k}}{\beta^*\omega y}, \frac{500v}{y^2\omega}\right), \frac{4\sigma_{\omega2}k}{CD_{k\omega}y^2}\right]\right\}^4\right\}$$

$$CD_{k\omega} = \max\left(2\rho\sigma_{\omega2}\frac{1}{\omega}\frac{\partial k}{\partial x_i}\frac{\partial \omega}{\partial x_i}, 10^{-10}\right)$$

$$F_2 = \tanh\left\{\left[\max\left(\frac{2\sqrt{k}}{\beta^*\omega y}, \frac{500v}{y^2\omega}\right)\right]^2\right\}$$

$$\alpha_1 = \frac{5}{9}, \alpha_2 = 0.44, \beta_1 = 0.075, \beta_2 = 0.0828 \text{ and } \beta^* = \frac{9}{10}$$

2.3. Particle tracking

When seawater is used as coolant in heat exchanger, the concentration of sand in the fluid is generally less than 1000 mg/kg. This is a fairly dilute particle concentration. Hence, the Lagrangian particle tracking approach was used in the present work to obtain timely information about particle concentration, velocity and impact factor by solving a finite number of particle trajectories statistically representing the particles moving in the fluid domain. The assumptions in this study include no particle collusion, no energy interaction between particles, no particle rotation, and rigid spherical particles. The particle equation of motion is then written as

$$\frac{d\vec{u_P}}{dt} = F_D\left(\vec{u} - \vec{u_P}\right) + \vec{g}\frac{\rho_P - \rho}{\rho_P} + F_{pg} + F_{vm} + F_{sl} \tag{5}$$

Where $\vec{u}$ and $\vec{u_p}$ are the fluid phase velocity and the particle velocity, respectively. ρ and ρ_p are the fluid density and the particle density. The left term is an additional acceleration (force/unit particle mass),

the first term at the right hand side is the drag force per unit particle mass and the second term is buoyancy. F_D is

$$F_D = \frac{18\mu}{\rho_p d_p^2} \frac{C_D Re}{24} \tag{6}$$

Here, μ is the molecular viscosity of the fluid and d_p is the particle diameter. Re is the relative Reynolds number, which is defined as

$$Re_p = \frac{\rho d_p |u_p - u|}{\mu} \tag{7}$$

As the fluid and particle concerned in the present work are water and sand, respectively, the virtual mass force, F_{vm}, and pressure gradient force, F_{pg}, are considered and they are given by

$$F_{vm} = 0.5 \frac{\rho}{\rho_p} \left(\vec{u}_p \nabla \vec{u} - \frac{d\vec{u}_p}{dt} \right) \tag{8}$$

And

$$F_{pg} = \frac{\rho}{\rho_p} \vec{u}_p \nabla \vec{u} \tag{9}$$

The shear lift force, F_{sl}, is also included in the force balance equation, which is expressed by

$$F_{sl} = \frac{2K\nu^{1/2} \rho d_{ij}}{\rho_p d_p (d_{lk} d_{kl})^{1/4}} \left(\vec{u} - \vec{u}_p \right) \tag{10}$$

where $K = 2.595$ and d_{ij} is the deformation tensor.

The particle position, r, is determined by solving its trajectory (Eq. (11)) by stepwise integration over discrete time steps. Integration in time of the particle motion equation gives the velocity vector of the particle at each point along the trajectory.

$$\frac{dr}{dt} = u_P \tag{11}$$

The dispersion of the particles due to turbulence velocity fluctuations is determined using a stochastic tracking method (random walk model) (ANSYS-Fluent, 2014). In the discrete random walk (DRW) model, the fluctuating velocity of particles is assumed to obey a Gaussian probability distribution and the interaction time of particles with the fluid phase eddy is determined by the smaller of eddy lifetime and the eddy crossing time. Numerical simulations have demonstrated that the erosion results predicted by the method agreed well with experimental data for large particles (Mansouri et al., 2015; Wong et al., 2013a,b) and employing the low-Re number approach significantly improved the erosion prediction for small particles (25 μm) (Mansouri et al., 2015). For particles with a diameter less than a few microns, the DRW model will show a tendency of slow particle velocity and particle concentration in near-wall low-turbulence regions, where the velocity fluctuations are not isotropic as in the bulk, especially, when one-way fluid-particle coupling approach is used. In the present work, the DRW model was also applied for particles of less than 10 μm to identify the difference to large particles. The influence of particle motion on the fluid flow field is included into the modelling, although this will led to about 50% increase in the computation time and has seldom been considered in previous studies for dilute solid-liquid systems (Badr et al., 2006; Parsi et al., 2014; Wong et al., 2013a,b). In the two-way coupling, the momentum gained or lost by the particles is incorporated in the subsequent continuous phase calculations (ANSYS-Fluent, 2014). The study on the effect of the two-way coupling on the dispersed and carrier phase turbulence fluctuations in a channel flow based on a direct numerical simulation has shown that, when the particle-fluid two-way coupling effect was accounted for, the particle normal fluctuating

velocity decreased near the wall, causing a decrease in the particle deposition velocity (Nasr et al., 2009).

2.4. Erosion modelling

There are many factors influence solid particle erosion, including the particle characteristics (shape, size, density, hardness and material), particle dynamics properties (velocity and motion direction to target surface) and target material properties (hardness and temperature). A number of experiments and concept analyses (such as cutting, low-cycle fatigue and adiabatic shear) on the relationship of erosion with these parameters led to a few models to predict the erosion (Njobuenwu and Fairweather, 2012; Parsi et al., 2014). Due to the complexity of the erosion process and the multiplicity of influence factors, the proposed models in a certain extent depend on the empirical coefficients extracted from various erosion experiments. There is no a general equation that can be used for all conditions. Five erosion models were chosen for predicting a pipe bend erosion by ductile particles (Njobuenwu and Fairweather, 2012). Although the magnitude of predicted erosion by the five models was different, they produced the similar erosion tendencies and can be considered in good agreement with the experimental data.

Erosion rate is an expression of mass loss of materials or thickness reduction of target in a specific period of time. As the linear dependence of erosion rate on the loaded particle mass in the dilute particle concentration range, mass (volume or thickness) loss per unit mass of feed particles (such as kg/kg) is also adopted. The unit used in this work is the metal loss per unit area in one second, mg/m^{2}s. The solid particle erosion model is described by the following general form

$$R_e = \sum_{p=1}^{N} \frac{\dot{m}_p C \left(d_p \right) f \left(\alpha \right) v^{b(v)}}{A_f} \tag{12}$$

where $C(d_p)$ is a function of particle diameter; α is the local particle impact angle, which is defined by the angle between particle motion direction and target wall; $f(\alpha)$ is a function of the particle impact angle that depends on target material; v is the local velocity of the impacting particle, $b(v)$ is the impact particle velocity power law coefficient being a function of velocity of the particle, typically it varies between 1.8 and 2.3 for ductile materials; A_f is the cell face area at the wall.

In the present work, the impact angle function $f(\alpha)$ for sand particles on carbon steel proposed by Wang and Shirazi (Y. Zhang et al., 2007) is used. The function is also used for copper, as the experimental evidence showing that the influence of particle impact angle on both materials is similar (Bitter, 1963a, 1963b; N. Lin et al., 2015).

$$f(\alpha) = \begin{cases} K_1 \alpha + K_2 \alpha^2 & \alpha \le \pi/12 \\ K_3 + K_4 \sin^2(\alpha) + K_5 \sin(\alpha)\cos^2(\alpha) & \alpha > \pi/12 \end{cases} \tag{13}$$

where K_i for $i = 1$–5 are empirical coefficients (Zhang et al., 2007).

The particle diameter function $C(d_p)$ can include the contribution of the properties of both particles and target materials, in addition to the particle diameter. Considering the relationship of erosion rate and particle diameter given by Oka et al. (Oka et al., 2005) and Oka and Yoshida (Oka and Yoshida, 2005), the particle diameter function is written by the following form.

$$C \left(d_p \right) = KB^{-n} F_s \left(\frac{d_p}{d_p^*} \right)^m \tag{14}$$

Where K is a material dependent constant; n and m are empirical coefficients; B is the Brinell hardness of wall; F_s is the particle sharpness factor; d_p and d_p^* are the particle diameter and the

reference particle diameter, respectively. The suggested values for F_s are 1.0 for sharp (angular), 0.53 for semi-rounded, or 0.2 for fully rounded sand particles. For SiO_2 particles on carbon steel $m = 0.19$ and $d^* = 326\,\mu$m were suggested (Oka et al., 2005; Oka and Yoshida, 2005). In an erosion model for a single particle, a power-law relation with an exponent of 0.5 was used for the effect of particle size on erosion rate (Huang et al., 2008).

2.5. Simulation details

The fluid domain was meshed using the tetrahedral grid, the size of the volume mesh was derived from the face meshes. Fine meshes, a size of 4 mm, were applied for the faces of tubes and the tube sheet, considering the small volume in the areas and strong turbulence of fluid in the tube entrances. The tube inside has 5 boundary layers with a first layer of 0.6 mm thickness and a transition ratio of 1.2. The head and the inlet pipe were also meshed to have 5 boundary layers. With the meshing scheme, the domain finally consists of almost 11.8×10^6 cells. The meshes were then improved by FLUENT mesh smooth function and finally have the maximum orthogonal skewness of 0.89, maximum aspect ratio of 52.60 and minimum orthogonal quality of 0.16. The grids were further refined using the solution-adaptive refinement feature in Fluent. The grid independence study for the model was performed by examining the values of y^+ and comparing the flow field in the head. The detail is discussed in Appendix A.

The simulations were performed with Ansys FLUENT version 16 (ANSYS-Fluent, 2014) with high order discretization of the equations. PRESTO was used for pressure, 3rd order Monotonic Upstream-centered Schemes for Conservation Laws (MUSCL) for continuity, momentum, k and ω equations. SIMPLE was used for the pressure-velocity coupling. As the k-ω has difficulty converging and is very sensitive to the initial values, the turbulent flow was first solved with steady k-ε model for 1000 iterations to find an initial condition for the k-ω solution. Initially the steady RANS and SST k-ω equations were applied. Due to the high value of RMS which highly vibrating at 1×10^{-2}, the unsteady equations as described before were used with a time step 0.1 s and 500 iterations for each step and it was found that the residuals can reduce to about 1×10^{-5}. The solution converges on identical results after about 20 steps, with unchanged shear stress on the tube sheet and fluid distribution through tube bundle. After the "steady flow" achieved, particles were then uniformly injected from over the inlet pipe boundary at a specified mass rate. The erosion rate was measured after 6 s unsteady simulation with the same time-step and convergence criteria as the simulations without particle injection.

In the present work the erosion caused by different size particles at different feed-water mass rates was simulated. As the short length of the inlet pipe, an initial velocity distribution with the one-seventh power-law velocity profile was used at the inlet pipe boundary. The turbulent intensity at the velocity inlet boundary was set at 5% and the length scale was set to 0.55 m. An outflow boundary condition was applied at the outlet of the porous plate.

3. Results

Erosion rates are calculated for tube sheet, the part of copper tube protruded outside the tube sheet and the surface of the copper tubes, since the practical evidence shows that these are the critical sections with respect to erosion. To demonstrate the dependence of erosion on flow pattern and solid particle behaviors close to the likely erosion areas, the impact angle, velocity and concentration of particles at upstream distance of 5 mm to the tube sheet, at the tube entrances and at tube inside 30 mm from the tube sheet are calculated from the particle trajectory. A wide range of particle size,
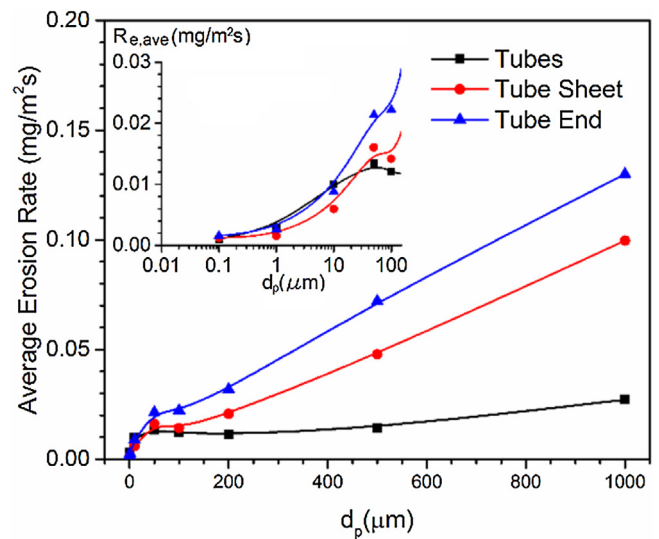

Fig. 3. Dependence of average erosion rates ($R_{e,ave}$) at the tube sheet, tube end and tube surface on particle size at feed flow rate of 210 m^3/h and loaded particle ratio of 856 mg/kg.

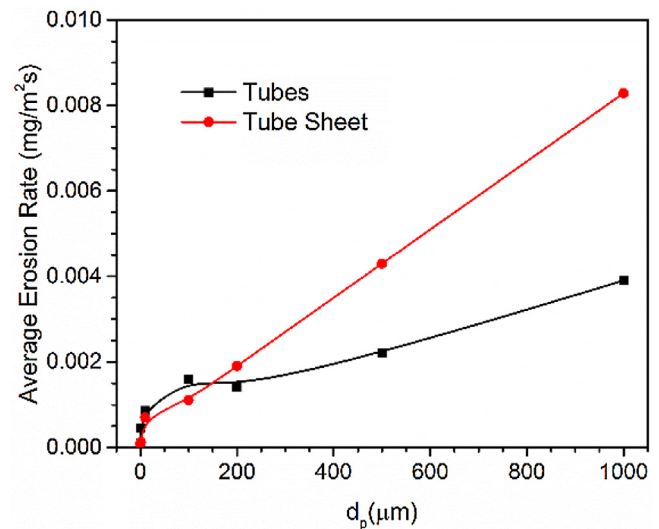**Fig. 4.** Dependence of average erosion rates at the tube sheet and tube surface on particle size at feed flow rate of 105 m^3/h and loaded particle ratio of 856 mg/kg.

from 0.1 to 1000 μm is considered, and the mass ratio of the loaded particles to the feed water at the inlet boundary of the inlet tube is from 1 mg/kg to about 850 mg/kg.

3.1. Erosion by different particles at different feed flow rates

Kinetic energy of particles impacting on wall dominates the erosion rate. For a specified particle, the size and impact speed are then the most important factors that influence erosion magnitude. In general, larger particles cause more severe erosion due to their higher kinetic energy, resulting in higher impact force to erode the surface. However, compared to the motion of particles in simple flow fields, such as, in straight pipes, elbows and sudden contraction, the erosion features on the metallic walls of a shell and tube heat exchanger are more complex as the size and velocity of particles impacting on a certain area much depend on the fluid flow field, particle density, shape and particle size itself. Figs. 3–6 show the erosion rates at tube sheet, tube ends in the inlet plenum and the inside surfaces of the tubes at different flow rates and different

particle sizes. The average rate is the facet average over the entire area of the concerned wall. The maximum rate is for the local area with the maximum facet-average erosion rate.

The simulation results show a near-linear dependence of the average erosion rate on the size of particles in the range of 100–1000 μm, an approximately the same erosion rates for the particles of 50–100 μm, and rapid decrease in the average erosion rate when the particle size reduces from 50 μm, as shown in Figs. 3 and 4. The dependence profile is in a good agreement with previous experiments (Clark, 1991; Desale et al., 2009; Gandhi and Borse, 2002). The linear relationship between erosion and particle size was found for glass beads on copper rod specimens (Clark, 1991), for sand on cast iron at 30° and 75° impact angles and at fluid velocity of 3.62 m/s and sand concentration of 20 wt% (Gandhi and Borse, 2002), and for 20 wt% silica sand on 6063 aluminum alloy at velocity of 3 m/s and 30° and 90° impact angles (Desale et al., 2009). The experiment on the metal loss caused by angular

SiC at fluid velocity of 20 m/s (Liebhard and Levy, 1991) indicated that the erosion ratio is nearly independent of particle size when the particles are larger than approximately 100 μm (Tilly, 1973). This relation was also found at a much higher velocity for a much stronger alloy (Tilly, 1973). Despite few experiments were reported for particles with the size of less than 50 μm, all of the above experiments showed a rapid decrease in the erosion rate with the size of small particles of less than 100 μm, as the present simulations predicted (inset in Figs. 3 and 4).

Tube ends in the inlet plenum underwent higher impingement at high velocity and large particles, compared to the tube sheet and tubes, as shown in Fig. 3. The erosion rate at the tube sheet is also higher than that at the tube surface when large particles are loaded (Figs. 3 and 4). When the particle size is reduced to less than about 100 μm, the average erosion rates at the tubes, the tube ends and the tube sheet are approximately the same (insert in Fig. 3). The erosion rate at the tubes is slightly higher than that at the tube sheet. This is easy to be understood if considering smaller particles tend to follow the liquid flow stream and enter into the tubes, while larger particles impact on the tube sheet and the tube ends.
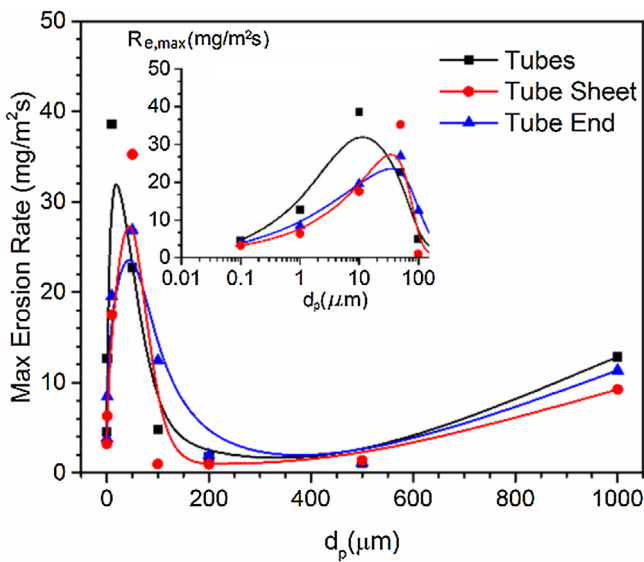

Fig. 5. Dependence of maximum erosion rates ($R_{e,max}$) at the tube sheet, tube end and tube surface on particle size at feed flow rate of 210 m^3/h and loaded particle ratio of 856 mg/kg.
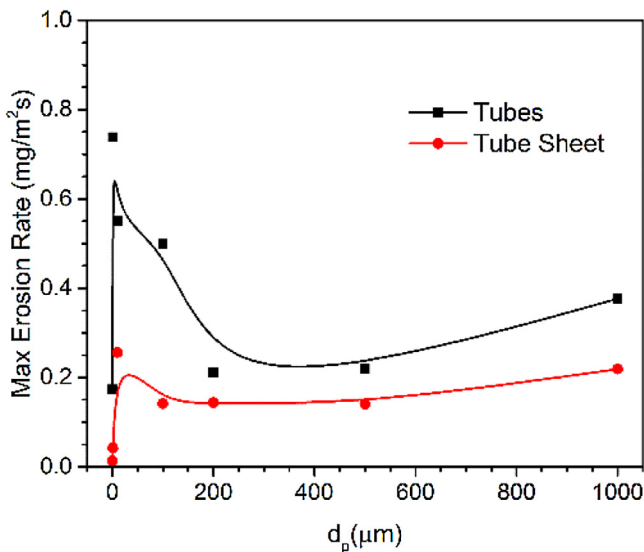

Fig. 7. Contour of fluid velocity at 5 mm upstream from the tube sheet at feed flow rate of 210 m^3/s.

Fig. 6. Dependence of maximum erosion rates at the tube sheet and tube surface on particle size at feed flow rate of 105 m^3/h and loaded particle ratio of 856 mg/kg.

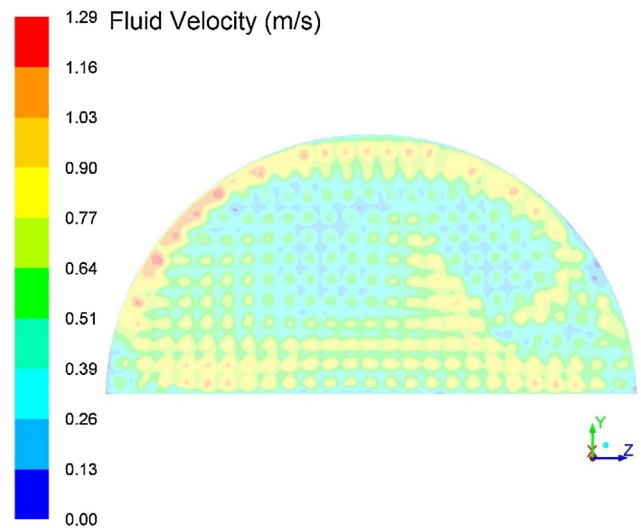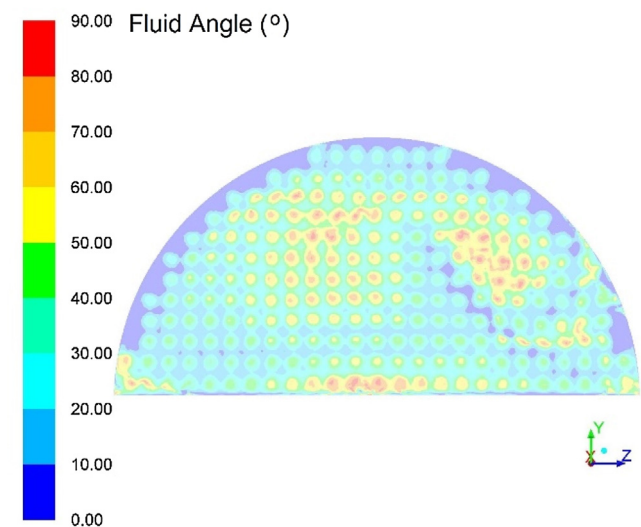**Fig. 8.** Flow angle relative to the plane of tube sheet at 5 mm upstream from the tube sheet at feed flow rate of 210 m^3/s.
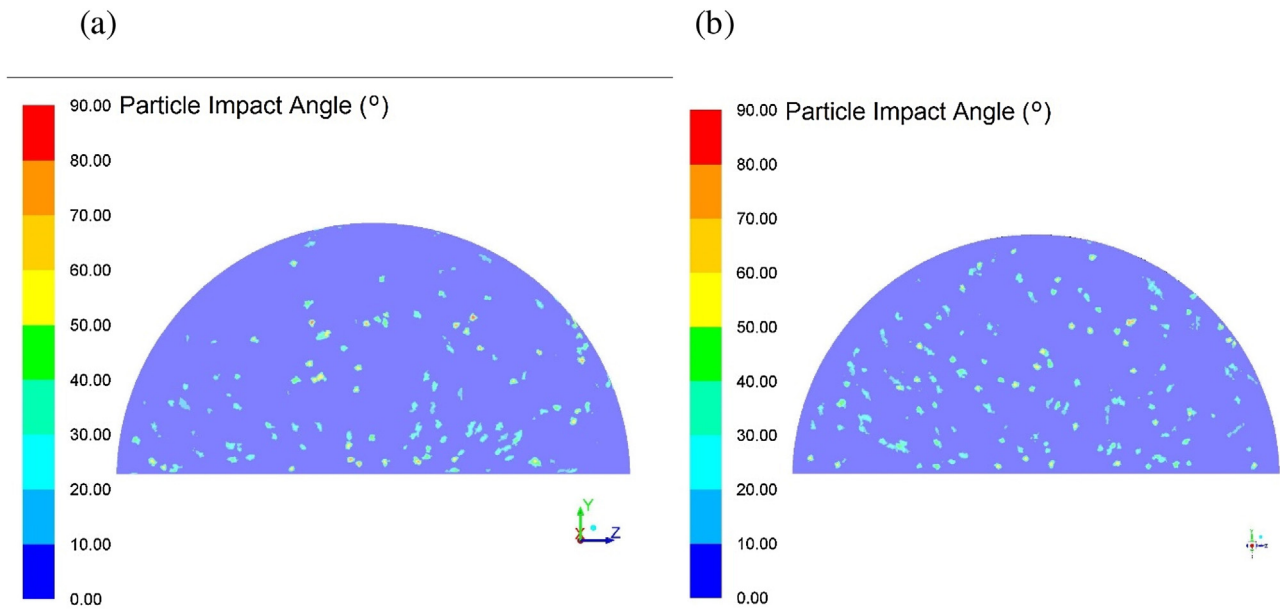
(a)　　　　　　　　　　　　　　　　　　　　(b)

Fig. 9. Impact angle of tracked particles of (a) 500 μm and (b) 100 μm on tube sheet at feed flow rate of 210 m³/h and particle ratio of 856 mg/kg.

(a)　　　　　　　　　　　　　　　　　　　　(b)
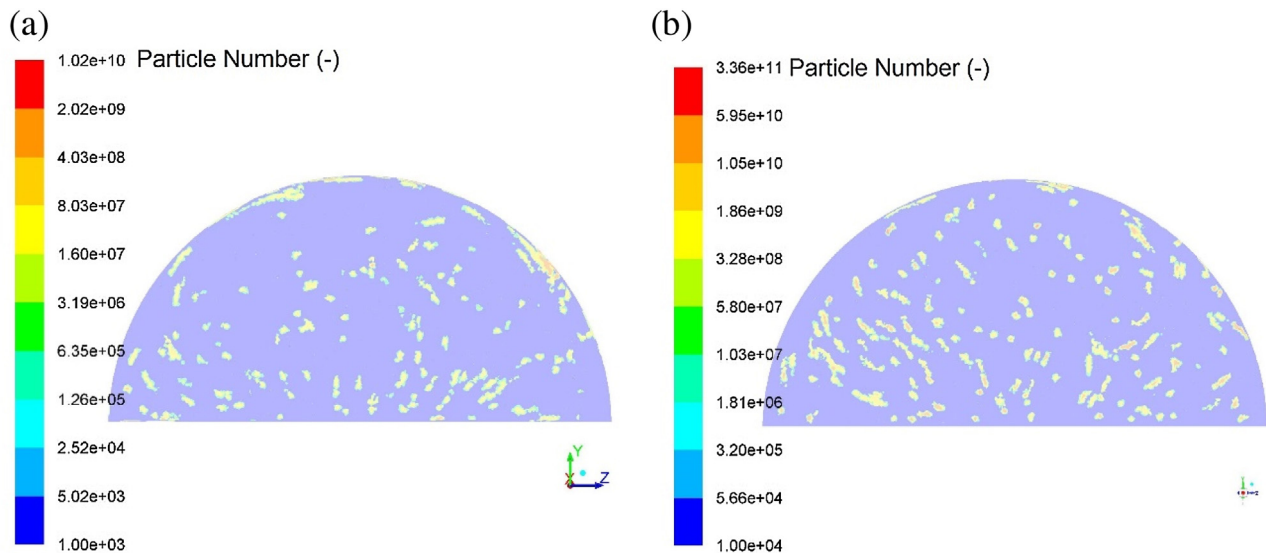
Fig. 10. The number density of (a) 500 μm and (b) 100 μm particles at 5 mm upstream from the tube at 210 m³/h feed flow rate and 856 mg/kg sand particle ratio.

The failure of shell and tube heat exchanger due to the erosion occurs at some local areas. The maximum local erosion rate was then calculated in the present work. The results are given in Figs. 5 and 6. Surprisingly, it was found that the highest erosion was produced by the particles with size of 10–50 μm. The similar results were also found in the simulation of sand particle erosion in a shell and tube heat exchanger at inlet flow velocity of 0.64 m/s (Habib et al., 2006), the highest erosion rate occurred when using sand particles of 100 μm diameter. This is because of the more efficient momentum exchange between fluid and smaller particles, resulting in higher particle velocity and larger mass (number) of particles presenting at some local regions (This will be discussed in the next section). The smaller particles in that range are more likely to flow with the fluid and gain a higher velocity, while the larger particles prefer to go straight ahead and deviate from the fluid stream due to their high inertia when the fluid encounters a wall and changes its flow direction in the head of the heat exchanger. Compared to the large particles, the small particles have a higher velocity and

more likely enter into the tubes with the fluid, causing severe erosions in the tubes (inset in Fig. 5). It is well known that the total kinetic energy of a group of particles with a specified total mass is a function of their velocity and size-independent. When small particles are loaded into the heat exchanger, the total kinetic energy of the particles is higher because of their higher velocity and larger amount of particles flowing with the fluid. The kinetic energy of the particles impacting on the wall dominates the erosion rate as the aforementioned.

In the present work 858 mg/kg solid particle concentration and even size distribution were used in the simulations. At such high particle loading rate, the 10 μm particles produced the maximum erosion rate of 38 mg/m²s in the tubes at 210 m³/h feed fluid. The maximum tube end and tube sheet erosion rates are also higher than 20 mg/m²s (insert in Fig. 5). When the heat exchanger is running at a lower feed fluid (105 m³/h) the maximum erosion rate decreased to 0.72 mg/m²s in the tubes and 0.25 mg/m²s at the tube sheet, indicating the dependence on the fluid velocity. The high
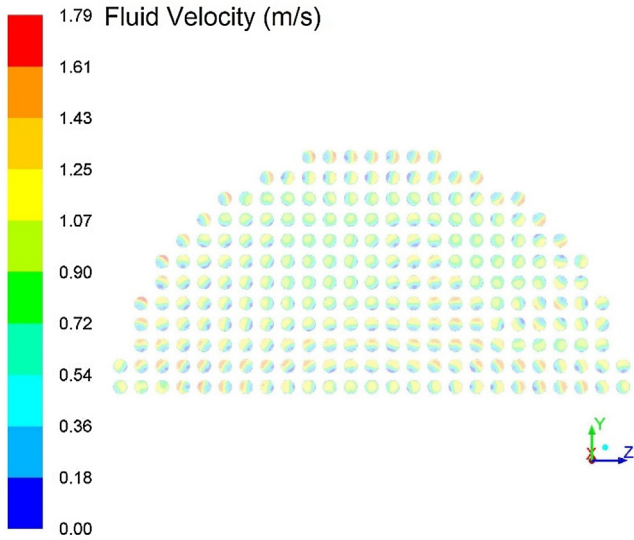
Fig. 11. Contour of fluid velocity in tubes at 30 mm from the tube sheet at feed flow rate of 210 m³/s.
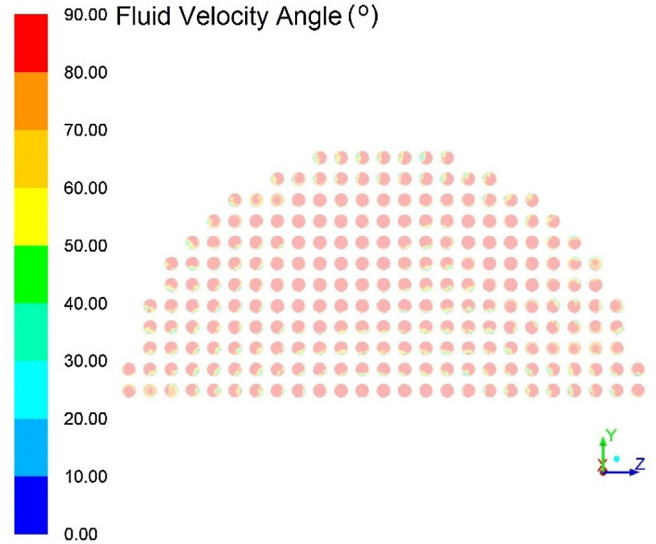
Fig. 12. Contour of fluid flow angle relative to tube axis in tubes at 30 mm from the tube sheet at feed flow rate of 210 m³/s. (flow streamline aligning with the tube axis has a flow angle of 90°).

erosion rates mean some tubes in the shell and tube heat exchanger would be damaged in a period of several weeks, fortunately, in practical the sand content in the feed fluid is not always such high and the portion of about 10 µm particles is also low.

3.2. Dependence on flow pattern and particle characteristics

The erosion much relies on the flow pattern and in some works only the flow simulation results are used to study the erosion process without modelling particle motion and erosion process itself (Bremhorst and Brennan, 2011). The flow angle and velocity magnitude are considered to be the dominant factors causing the particle erosion. In the present work both the flow pattern and the particle behaviors are analyzed with respect to their influence on the erosion.

The velocity magnitude and flow direction are presented in Figs. 7 and 8, respectively. The magnitude and direction contours indicate the flow kinetic energy and mass distribution across the

tube sheet. It seems that the areas with high velocity and relatively low flow angle are likely to be eroded, as the maximum erosion wear occurs at the impact angle of about 20° for sand particles impacting on carbon steel and copper (Bitter, 1963a, 1963b; Lin et al., 2015). However, the contour of impact angle of large particles (500 µm, Fig. 9a) shows that the particle impact angle is inconsistent with the flow direction. Particles in most regions with high flow angle have a low impact angle and the particle number density is high in these regions (Fig. 10a). Whereas a few large particles were found in the region with high flow velocity and the angle that can cause high erosion rate. For small particles (100 µm) the impact angle contour (Fig. 9b) is approximately consistent with the flow direction (Fig. 8) and more particles move into the top region with the fluid (Fig. 10b). This indicates the likelihood of separation of large particles from the fluid streamlines and the failure position of the heat exchanger depends on the particle size distribution.

(a)

(b)
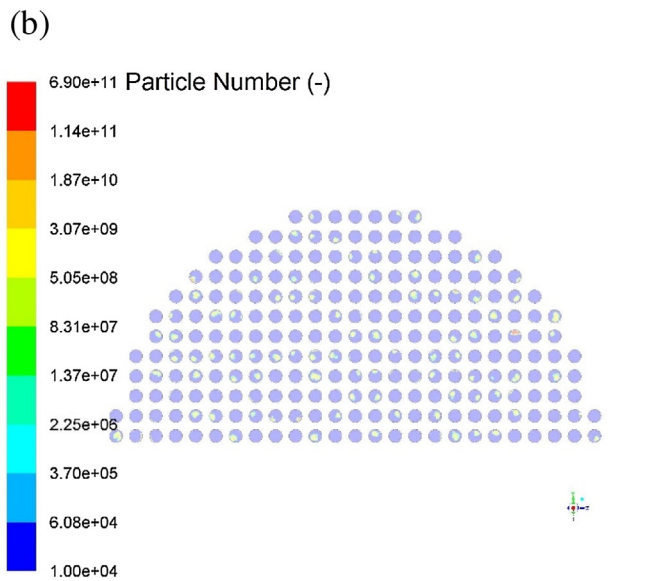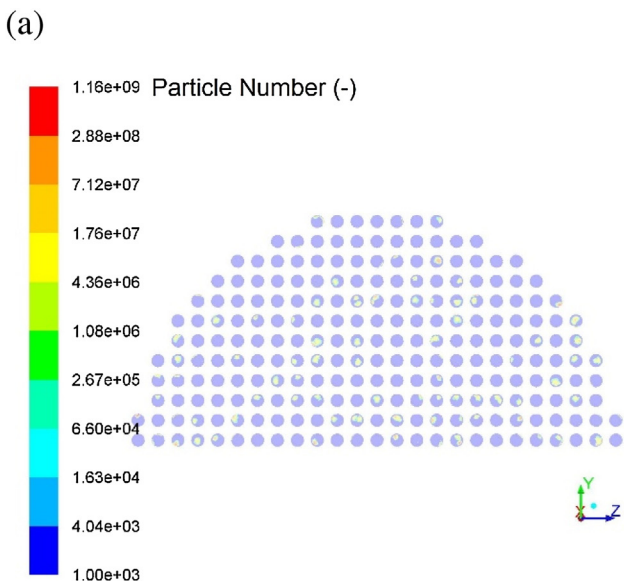
Fig. 13. The number density of (a) 500 µm and (b) 100 µm particles in the tubes at 30 mm from the tube sheet at 210 m³/h feed flow rate and 856 mg/kg particle ratio.
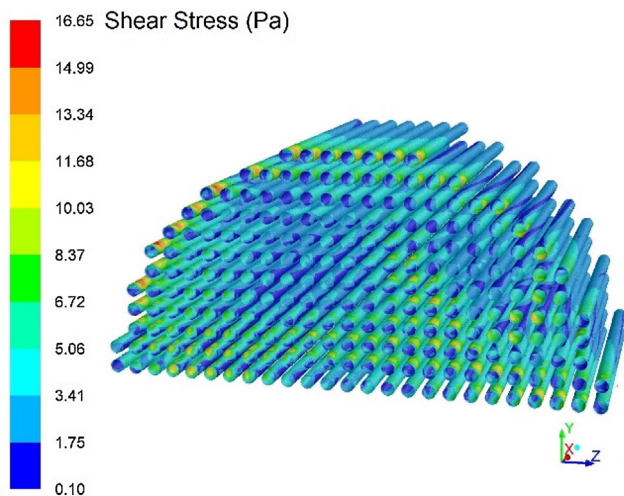
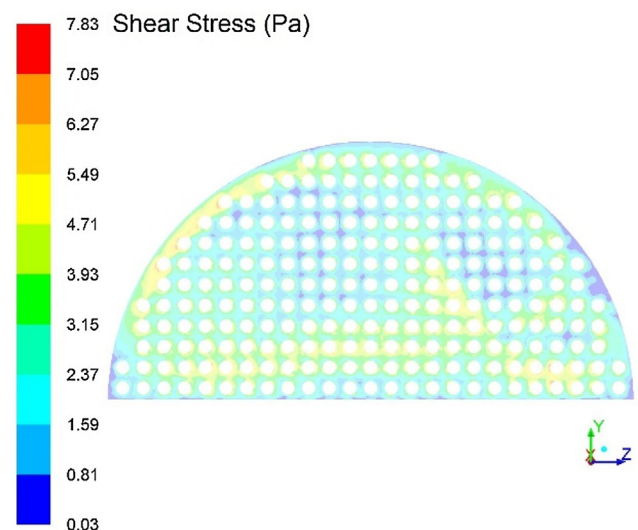**Fig. 14.** Shear stress at the tubes at feed flow rate of $210\,\mathrm{m^3/s}$.

Fig. 15. Shear stress at the tube sheet at feed flow rate of $210\,\mathrm{m^3/s}$.

The large particles tend to sweep into the corner between the tube sheet and the semi-circular head wall (Fig. 10 a) and flow into the 3 bottom-row tubes and the tubes located in the area with flow direction aligning with the tube axis in the heat exchanger (Fig. 13a). In the flow development section of these tubes the flow velocity is low (Fig. 11) and the direction of all flow streamlines across the tube section is about 90° (Fig. 12). It was found that the contour of particle direction was approximately consistent with the fluid flow, indicating an impact angle of 0°. The particle motion characteristics led to the average erosion rate (Fig. 3) and the maximum erosion rate (Fig. 5) are not as high as that could be caused by the high particle number density in the tubes (Fig. 13a).

The difference in the erosion rate between the tubes and tube sheet, caused by small particles, is not as obvious as that caused by the large particles at $210\,\mathrm{m^3/h}$ feed flow rate (Fig. 3). On the contrary, the tube erosion caused by the small particles (less than around $100\,\mu\mathrm{m}$ at $210\,\mathrm{m^3/h}$ (Fig. 3), less than around $150\,\mu\mathrm{m}$ at $105\,\mathrm{m^3/h}$ (Fig. 4)) is larger than the tube sheet erosion rate. This is attributed to the characteristics of the small particle motion. Figs. 10b and 13b show more small particles entering into the tubes where the fluid flow produced higher shear stress on the tube surface (Fig. 14). Moreover, the average shear stress on the tube surface (Fig. 14) is higher than that on the tube sheet (Fig. 15).

3.3. Flow-field comparison with large eddy simulations

The SST has proven to give reliable predictions in a wide range of applications and is therefore commonly used for most engineering flow problems (Menter et al., 2003; Versteeg and Malalasekera, 2007). Nevertheless, concerning the verification and validation of the solution and the difficulty in experimental observation, large eddy simulation (LES) was employed to verify the results of the RANS SST k-ω model. Generally the LES model can yield better result than the RANS models for separated flow and recirculating flow, however it requires much finer meshes and shorter time steps and, therefore, significantly high costs in terms of compute power and run times. In the present work, LES is conducted on the same mesh as for the RANS simulation, wherein y^+ is up to 35 at some first cells to the wall of the tubes and it is in the range of 0.5–18 for the wall-adjacent cells of the tube sheet and the head wells. The mesh is too coarse for LES to resolve the near-wall flow structure in the viscous sublayer and the buffer layer. Wall Modeled LES (WMLES) (Shur et al., 2008) was therefore used in the present work, which can tolerate large y^+ values and reduces the grid resolution
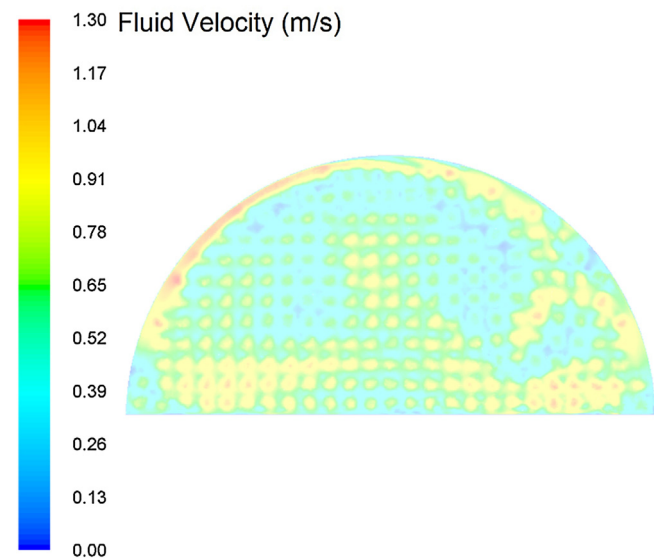

Fig. 16. Fluid velocity obtained by LES for 5 mm upstream from the tube sheet at feed flow rate of $210\,\mathrm{m^3/s}$.

requirements relative to the boundary layer thickness to be largely Reynolds number-independent for channel and pipe flows. The LES simulation was performed for 3 s at a time step of 5×10–4 s (the estimated CFL<0.3), starting from an initial flow field from the RANS computation.

The flow field in terms of velocity and flow angle in the head close to the tube sheet was first examined (Fig. 16 and 17). They clearly show approximately the same results as the RANS SST k-ω model (Figs. 7 and 8), albeit the LES predicted slightly higher velocities in the center of the head than the RANS simulations. The LES also produced a roughly left-right symmetrical flow field in this region as shown in Figs. 16 and 17. Far from the tube sheet, high velocities around the outer wall of the head and flow inclination to one side were observed as that from RANS (Fig. 18). The flow volume rate through each tube was also calculated (Fig. 19), which represents the overall influence of the resulting flow behaviors in the entire heat exchanger and is most important for assessing the
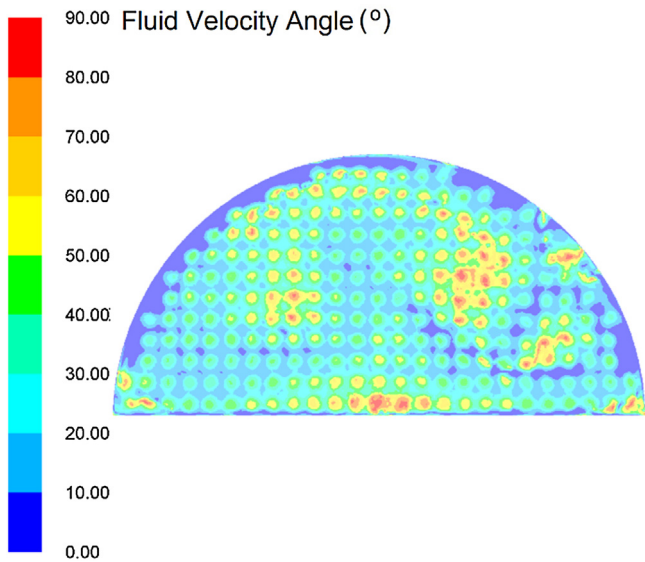
Fig. 17. Flow angle relative to the plane of tube sheet at 5 mm upstream from the tube sheet for LES at feed flow rate of 210 m³/s.

heat exchanger design and the solid particle erosion. It was found that the LES and the RANS simulations produced very close results for all the tubes.

4. Conclusions

The erosion of a two-pass shell and tube heat exchanger was simulated by modelling the flow and particle motion with a physical model, where each individual tube was presented by a short tube plus a porous plug and a porous plate was used to adjust the backpressure in the rear head. This approach revealed more flow aspects affecting the erosion of the head and tubes of the heat exchanger, compared to the treating not including the modelling of flow in the rear head and the second pass. The model includes both the flow field in the development section of each tube and the deviation of flow rates through the tubes into the affecting parameters on erosion.

The fluid flow was described with RANS and SST-k-ω turbulence models, while the sand particles in the shell and tube heat exchanger were investigated using the Lagrangian particle tracking method. The erosion was predicted for sand particles of 0.1 to 1000 μm in diameter. It was found that the erosion caused by large particles was inconsistent with the flow pattern due to the separation of the particles having high inertia from the flow stream, when the flow direction changes, while the erosion due to small particles
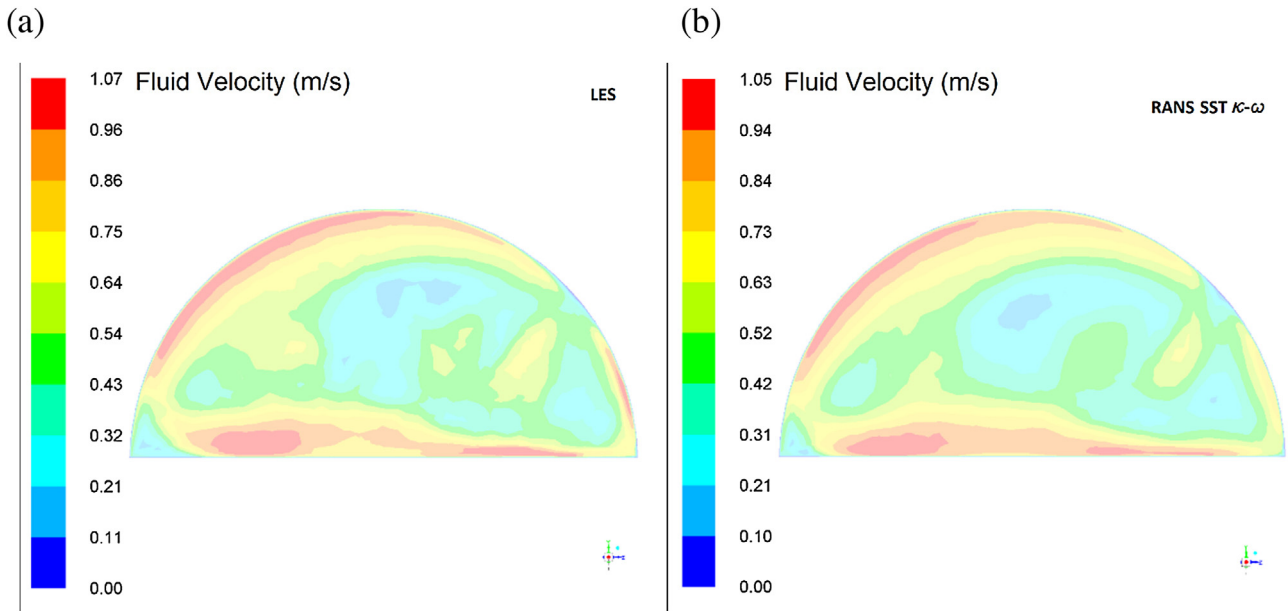
(a)   (b)

Fig. 18. Comparison of the distribution of fluid velocity (m/s) obtained by (a) LES and (b) RANS at 100 mm upstream from the tube sheet at feed flow rate of 210 m³/s.

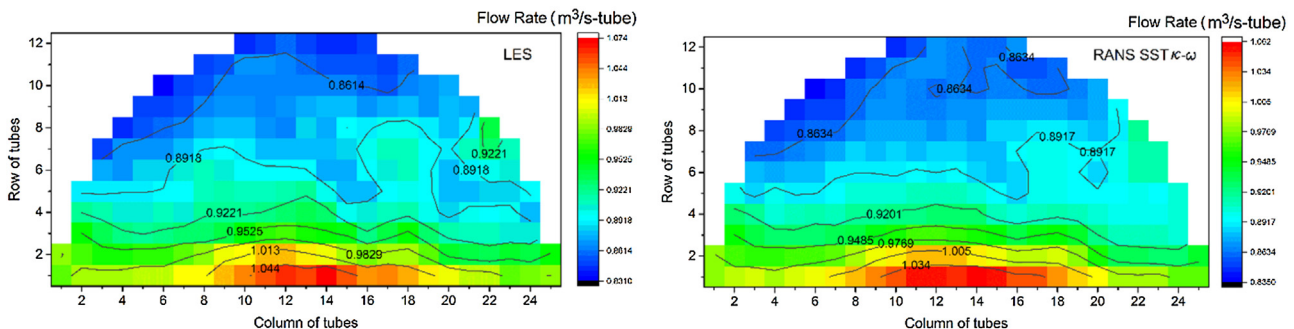**Fig. 19.** Distribution of flow rate through the tubes at feed flow rate of 210 m³/s.

of less than 100 μm can be represented by the flow characteristics, such as the flow direction and velocity magnitude.

The erosion rates of tube sheet and the tube ends in the inlet head have a near-linear relation to the particles of more than 200 μm, while the tube erosion rate is almost independent on particle size, slightly increasing with the increase in particle size. The erosion rates are independent on the size of small particles (50–200 μm) and are approximately the same at tube sheet and tube surfaces. The predicted relationship of erosion rate and particle size is in a good agreement with experiments. When particles of less than 50 μm were loaded into the heat exchanger, the average erosion rates at tube sheet and tube surfaces rapidly decreased with the particle size, whereas the fine particles produced very high erosion at some local areas. Based on the dependences of the erosion rates of tube sheet and tubes on the particle size, the particles can be classified into three groups, i.e., large particles with diameter of more than 200 μm, small particles in the range of about 50–200 μm and fine particles of less than about 50 μm. This result is significant for controlling the corresponding size particles loaded into the heat exchanger to reduce its erosion.

It was found that the maximum local erosion rate at both the tube sheet and the tubes caused by 10 μm particles was about 10–20 times of that produced by 200 μm particles. The maximum tube erosion rate reached about 38 mg/m^{2}s at feed fluid rate of 210 m^3/s and loading 856 mg particles per kilogram fluid. Note that the high erosion rates caused by small particles may be attributed to the overprediction of the concentration of the small particles on the walls, which is an inherent problem of the DRW model due to its isotropic treatment of the normal to the wall fluctuation, although the low-Re number approach and two-way coupling were adapted to ease the problem in the present work. Given the comparison of the present simulation results with limited previous works and the absence of experimental validation, the results are more qualitative than quantitative.

Acknowledgment

Appendix A. : Grid independence study

The grid independence study is mainly to examine the influence of grid size on the prediction of flow behavior, especially, in the regions close to the tube sheet and the flow development regions in the tubes. As there are 230 tubes of 20 mm in diameter and 600 mm in length in the heat exchanger model, an efficient mesh is expected to capture the local turbulent features and provide reliable solution within an acceptable computational time. In the study, the values of y$^+$ were utilized for examining the mesh quality in the viscous layer near the wall, focusing on the layers near the tube sheet and the tube walls. Meanwhile the flow field was used for surveying the mesh quality in the head of the heat exchanger.

Initially, 0.6 mm and 2 mm were applied for the first layer near the tube walls and the head walls, respectively. The SST k-ω simulation predicts that y$^+$ at some walls of the tubes is in the log-law region. The boundaries were then refined and the values of y$^+$ at the wall-adjacent cells are in the viscous sublayer. It was also found that a very small cell height (<0.1 mm) at the flow development region in some tubes is required to approach y$^+$ = 1 at the walls, due to the fact of the rapid changes in geometry and the shear layers with large strain rates. So that most of y$^+$ are finally controlled in the viscous sublayer and the low-Re formulation was used to resolve the sublayer in the simulation. For the wall-adjacent cells of y$^+$ > 5, wall functions were automatically used by the SST k-ω model.

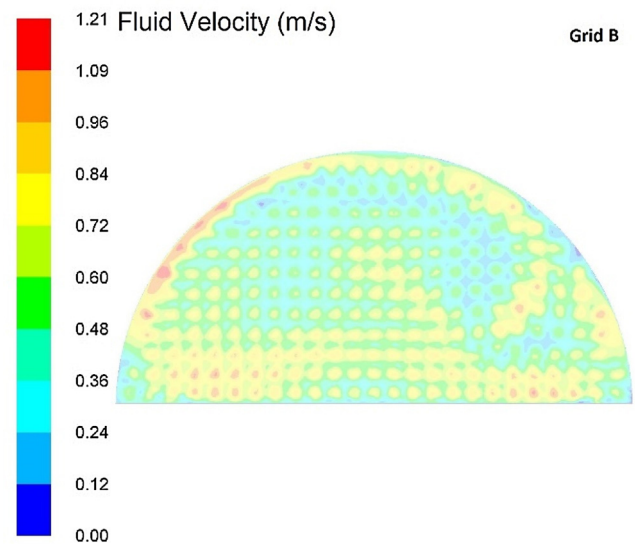**Fig. 20.** Contour of fluid velocity (m/s) at 5 mm upstream from the tube sheet at feed flow rate of 210 m^3/s (Grid B), comparable to the results of Grid A shown in Fig. 7.

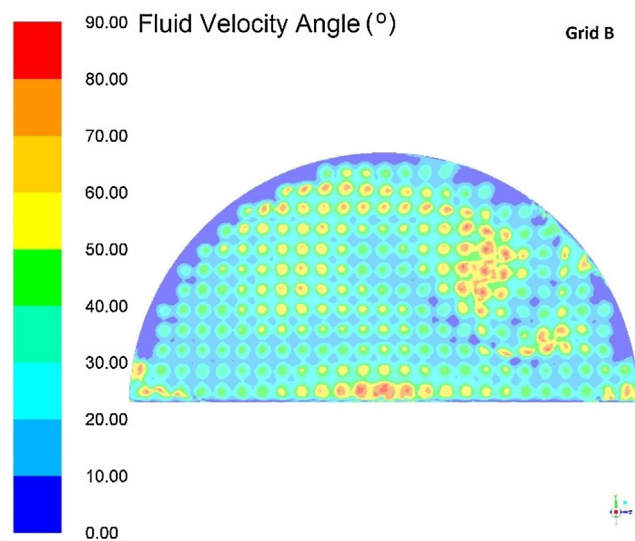**Fig. 21.** Flow angle relative to the plane of tube sheet at 5 mm upstream from the tube sheet at feed flow rate of 210 m^3/s (Grid B), comparable to the results of Grid A shown in Fig. 8.

The grid was refined by the use of the solution-adaptive mesh refinement feature of Fluent (ANSYS-Fluent, 2014). The method can add additional cells where required, which is in this case in the regions close to the tube sheet and in the tubes and the regions predicted to have high velocity gradients. In order to assess how much the flow field depends on the supplementary cells, the simulations were repeated after the refinement. The results of the last refined grid (Grid B) were presented in Figs. 20–23 and compared with these of the grid (Grid A) used in the main section of this paper. It can be seen that the velocity distribution (Fig. 20) and flow angle (Fig. 21) 5 mm upstream of the tube sheet predicted by Grad B are comparable to the results of Grad A (Fig. 7 and Fig. 8). The last refinement did not have a significant effect on the results for the most important flow regions in this case. Figs. 22 and 23 compare the
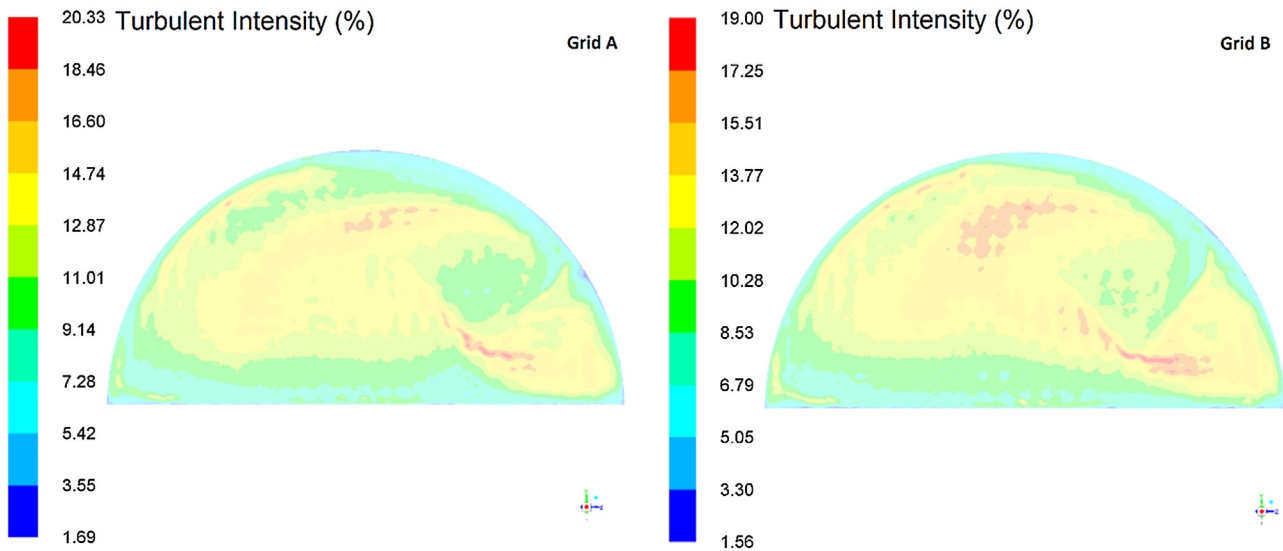
Fig. 22. Turbulent intensity (%) at 5 mm upstream from the tube sheet at feed flow rate of 210 m^3/s.

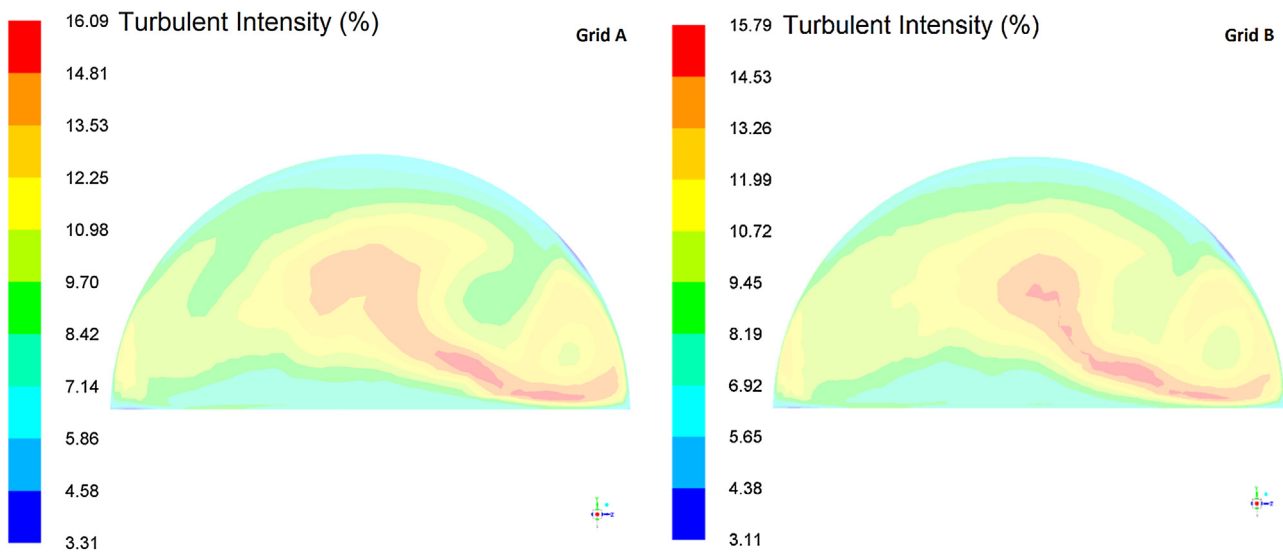**Fig. 23.** Turbulent intensity (%) at 100 mm upstream from the tube sheet at feed flow rate of 210 m^3/s.

turbulence in the head, showing the results for both grids are very similar.

References

ANSYS-Fluent, 2014. User's Guide Release 16.0. ANSYS Inc.

Badr, H.M., Habib, M.A., Ben-Mansour, R., Said, S.A.M., 2005. Numerical investigation of erosion threshold velocity in a pipe with sudden contraction. Comput. Fluids 34, 721–742.

Badr, H.M., Habib, M.A., Ben-Mansour, R., Said, S.A.M., Al-Anizi, S.S., 2006. Erosion in the tube entrance region of an air-cooled heat exchanger. Int. J. Impact Eng. 32, 1440–1463.

Aslam Bhutta, M.M., Hayat, N., Bashir, M.H., Khan, A.R., Ahmad, K.N., Khan, S., 2012. CFD applications in various heat exchangers design: a review. Appl. Therm. Eng. 32, 1–12.

Bitter, J.G.A., 1963a. A study of erosion phenomena. Wear 6, 169–190.

Bitter, J.G.A., 1963b. A study of erosion phenomena part I. Wear 6, 5–21.

Bremhorst, K., Brennan, M., 2011. Investigation of shell and tube heat exchanger tube inlet wear by computational fluid dynamics. Eng. Appl. Comput. Fluid Mech. 5, 566–578.

Bremhorst, K., Lai, J.C.S., 1979. The role of flow characteristics in corrosion-erosion of tube inlets in the inlet channel of shell and tube heat exchangers. Wear 54, 87–100.

Chen, X., McLaury, B.S., Shirazi, S.A., 2004. Application and experimental validation of a computational fluid dynamics (CFD)-based erosion prediction model in elbows and plugged tees. Comput. Fluids 33, 1251–1272.

Clark, H.M., 1991. On the impact rate and impact energy of particles in a slurry pot erosion tester. Wear 146, 165–183.

Desale, G.R., Gandhi, B.K., Jain, S.C., 2009. Particle size effects on the slurry erosion of aluminium alloy (AA 6063). Wear 266, 1066–1071.

Duwig, C., Salewski, M., Fuchs, L., 2008. Simulations of a turbulent flow past a sudden expansion: a sensitivity analysis. AIAA J. 46, 408–419.

Gandhi, B.K., Borse, S.V., 2002. Effect of particle size and size distribution on estimating erosion wear of cast iron in sand-water slurries. Indian J. Eng. Mater. Sci. 09, 480–486.

Habib, M.A., Ben-Mansour, R., Badr, H.M., Said, S.A.M., Al-Anizi, S.S., 2005. Erosion in the tube entrance region of a shell and tube heat exchanger. Int. J. Numer. Methods Heat Fluid Flow 15, 143–160.

Habib, M.A., Badr, H.M., Said, S.A.M., Ben-Mansour, R., Al-Anizi, S.S., 2006. Solid-particle erosion in the tube end of the tube sheet of a shell-and-tube heat exchanger. Int. J. Numer. Methods Fluids 50, 885–909.

Habib, M.A., Badr, H.M., Ben-Mansour, R., Kabir, M.E., 2007. Erosion rate correlations of a pipe protruded in an abrupt pipe contraction. Int. J. Impact Eng. 34, 1350–1369.

Habib, M.A., Ben-Mansour, R., Badr, H.M., Kabir, M.E., 2008. Erosion and penetration rates of a pipe protruded in a sudden contraction. Comput. Fluids 37, 146–160.

Huang, C., Chiovelli, S., Minev, P., Luo, J., Nandakumar, K., 2008. A comprehensive phenomenological model for erosion of materials in jet flow. Powder Technol. 187, 273–279.

Kesana, N.R., Grubb, S.A., McLaury, B.S., Shirazi, S.A., 2013a. Ultrasonic measurement of multiphase flow erosion patterns in a standard elbow. J. Energy Resour. Technol. 135, 032905–032905.

Kesana, N.R., Throneberry, J.M., McLaury, B.S., Shirazi, S.A., Rybicki, E.F., 2013b. Effect of particle size and liquid viscosity on erosion in annular and slug flow. J. Energy Resour. Technol. 136, 012901–012901.

Kuźnicka, B., 2009. Erosion–corrosion of heat exchanger tubes. Eng. Fail. Anal. 16, 2382–2387.

Laguna-Camacho, J. R., Vite-Torres, M., Gallardo-Hernández, E. A., & Vera-Cárdenas, E. E., (2013). Solid Particle Erosion on Different Metallic Materials. In D. H. Pihtili (Ed.), Tribology in Engineering: InTech.

Lai, J.C.S., Bremhorst, K., 1979. Control of corrosion-erosion of tube inlets of shell and tube heat exchangers. Wear 54, 101–112.

Liebhard, M., Levy, A., 1991. The effect of erodent particle characteristics on the erosion of metals. Wear 151, 381–390.

Lin, Z., Ruan, X., Zhu, Z., Fu, X., 2014. Numerical study of solid particle erosion in a cavity with different wall heights. Powder Technol. 254, 150–159.

Lin, N., Lan, H.-Q., Xu, Y.-G., Cui, Y., Barber, G., 2015. Coupled effects between solid particles and gas velocities on erosion of elbows in natural gas pipelines. Procedia Eng. 102, 893–903.

Mansouri, A., Arabnejad, H., Karimi, S., Shirazi, S.A., McLaury, B.S., 2015. Improved CFD modeling and validation of erosion damage due to fine sand particles. Wear 338–339, 339–350.

Mazumder, Q.H., Shirazi, S.A., McLaury, B.S., 2008. Prediction of solid particle erosive wear of elbows in multiphase annular flow-model development and experimental validations. J. Energy Resour. Technol. 130, 023001–023001.

Menter, F., Kuntz, M., Langtry, R., (2003). Ten years of industrial experience with the SST turbulence model.

Mishra, S., Jayaraman, K., 2002. Asymmetric flows in planar symmetric channels with large expansion ratio. Int. J. Numer. Methods Fluids 38, 945–962.

Nasr, H., Ahmadi, G., McLaughlin, J.B., 2009. A DNS study of effects of particle?particle collisions and two-way coupling on particle deposition and phasic fluctuations. J. Fluid Mech. 640, 507–536.

Naz, M.Y., Ismail, N.I., Sulaiman, S.A., Shukrullah, S., 2015. Electrochemical and dry sand impact erosion studies on carbon steel. Sci. Rep. 5, 16583.

Nemitallah, M.A., Ben-Mansour, R., Habib, M.A., Ahmed, W.H., Toor, I.H., Gasem, Z.M., Badr, H.M., 2014. Solid particle erosion downstream of an orifice. J. Fluids Eng. Trans. ASME 137.

Njobuenwu, D.O., Fairweather, M., 2012. Modelling of pipe bend erosion by dilute particle suspensions. Comput. Chem. Eng. 42, 235–247.

Oka, Y.I., Yoshida, T., 2005. Practical estimation of erosion damage caused by solid particle impact: part 2: mechanical properties of materials directly associated with erosion damage. Wear 259, 102–109.

Oka, Y.I., Okamura, K., Yoshida, T., 2005. Practical estimation of erosion damage caused by solid particle impact: part 1: effects of impact parameters on a predictive equation. Wear 259, 95–101.

Parsi, M., Najmi, K., Najafifard, F., Hassani, S., McLaury, B.S., Shirazi, S.A., 2014. A comprehensive review of solid particle erosion modeling for oil and gas wells and pipelines applications. J. Nat. Gas Sci. Eng. 21, 850–873.

Ranjbar, K., 2010. Effect of flow induced corrosion and erosion on failure of a tubular heat exchanger. Materials & Design 31, 613–619.

Research & Markets, (2011). Research and Markets: Uhlig's Corrosion Handbook, 3rd Edition. In.

Safaei, M.R., Mahian, O., Garoosi, F., Hooman, K., Karimipour, A., Kazi, S.N., Gharehkhani, S., 2014. Investigation of micro- and nanosized particle erosion in a 90° pipe bend using a two-phase discrete phase model. Sci. World J. 2014, 12.

Shi, Y.-L., Ji, J.-J., Zhang, C.-L., 2010. Semiporous media approach for numerical simulation of flow through large-scale sparse tubular heat exchangers. HVAC R Res., 617.

Shur, M.L., Spalart, P.R., Strelets, M.K., Travin, A.K., 2008. A hybrid RANS-LES approach with delayed-DES and wall-modelled LES capabilities. Int. J. Heat Fluid Flow 29, 1638–1649.

Sugawara, K., Yoshikawa, H., Ota, T., 2005. LES of turbulent separated flow and heat transfer in a symmetric expansion plane channel. J. Fluids Eng. 127, 865–871.

Ternik, P., 2009. Planar sudden symmetric expansion flows and bifurcation phenomena of purely viscous shear-thinning fluids. J. Non-Newtonian Fluid Mech. 157, 15–25.

Tilly, G.P., 1973. A two stage mechanism of ductile erosion. Wear 23, 87–96.

Velasco, F.J.S., del Prá, C.L., Herranz, L.E., 2008. Expansion of a radial jet from a guillotine tube breach in a shell-and-tube heat exchanger. Exp. Therm. Fluid Sci. 32, 947–961.

Versteeg, H.K., Malalasekera, W., 2007. An Introduction to Computational Fluid Dynamics: the Finite Volume Method. Pearson Education.

Wong, C.Y., Solnordal, C., 2012. Minimising solid particle erosion in an annular cavity. In: Advances in Applied Mechanics Research, Conference Proceedings – 7th Australasian Congress on Applied Mechanics, ACAM 2012, pp. 627–636.

Wong, C.Y., Solnordal, C., Swallow, A., Wang, S., Graham, L., Wu, J.1, 2012. Predicting the material loss around a hole due to sand erosion. Wear 276–277, 1–15.

Wong, C.Y., Solnordal, C., Swallow, A., Wu, J., 2013a. Experimental and computational modelling of solid particle erosion in a pipe annular cavity. Wear 303, 109–129.

Wong, C.Y., Solnordal, C., Swallow, A., Wu, J., 2013b. Experimental and computational modelling of solid particle erosion in a pipe annular cavity. Wear 303, 109–129.

Zhang, H., Tan, Y., Yang, D., Trias, F.X., Jiang, S., Sheng, Y., Oliva, A., 2012. Numerical investigation of the location of maximum erosive wear damage in elbow: effect of slurry velocity, bend orientation and angle of elbow. Powder Technol. 217, 467–476.

Zhang, Y., Reuterfors, E.P., McLaury, B.S., Shirazi, S.A., Rybicki, E.F., 2007. Comparison of computed and measured particle velocities and erosion in water and air flows. Wear 263, 330–338.